

Article

Removal of Methylene Blue from Water by BiFeO₃/Carbon Fibre Nanocomposite and Its Photocatalytic Regeneration

Shuang Jiao ¹, Yiming Zhao ¹, Meng Bi ¹, Shuyue Bi ², Xiangman Li ³, Binsong Wang ^{1,*},
Chensha Li ^{4,*} and Yinmao Dong ^{5,*}

¹ Key Laboratory of Chemical Engineering Process and Technology for High-Efficiency Conversion, School of Chemistry and Material Sciences, Heilongjiang University, Harbin 150080, China; jiaoshuang92@126.com (S.J.); zym14704504925@163.com (Y.Z.); hrb921015@163.com (M.B.)

² College of Medicine Information Technology, Heilongjiang University of Chinese Medicine, Harbin 150040, China; zym15246852594@163.com

³ Women and Children Health Centre of Xiangfang District, Harbin 150040, China; huwentaolxm@163.com

⁴ Key Laboratory of Functional Inorganic Material Chemistry, Ministry of Education of the People's Republic of China, Heilongjiang University, Harbin 150080, China

⁵ Key Laboratory of Plant Resource Research and Development, School of Sciences/Beijing, Beijing Technology and Business University, Beijing 100048, China

* Correspondence: wangbinsong@hlju.edu.cn (B.W.); lichensha@hlju.edu.cn (C.L.); dongym@th.btbu.edu.cn (Y.D.)

Received: 25 April 2018; Accepted: 26 June 2018; Published: 29 June 2018



Abstract: It is essential to prepare a highly efficient and reproducible adsorbent for purifying industrial dye wastewater. In this work, a novel and efficient BiFeO₃/carbon fiber (CCT-BFO) nanocomposite adsorbent was prepared by the template method and through optimizing the preparation process. The morphology, physicochemical properties, and specific surface characteristics of the CCT-BFO were characterized by scanning electron microscope (SEM), transmission electron microscopy (TEM), X-ray diffraction (XRD) patterns, Fourier-transform infrared spectrometer (FTIR), and N₂ adsorption-desorption isotherm. The CCT-BFO could efficiently remove the Methylene blue (MB) from aqueous solutions, and the adsorption performance is not easily influenced by the environment. The equilibrium adsorption data were fitted to the classical models very well; the maximum capacity of adsorption MB onto the CCT-BFO was higher than many other reported adsorbents and the data of the adsorption kinetics were described by a pseudo-second-order model. Furthermore, the CCT-BFO can be recycled by photocatalytic regeneration. And the constant adsorption capacity was almost retained after recycling five times.

Keywords: bismuth ferrate; carbon fiber; methylene blue; adsorption; photocatalysis; regeneration

1. Introduction

With the rapid development of the industries, the problem of water pollution has become increasingly serious. Many types of industrial wastewater have been produced and discharged [1]. Among them, the dyeing wastewater produced by the manufacturers of dye productions, textiles, papermaking, leather, cosmetics, and plastics, etc., possess a serious threat to humans, animals, and plants [2]. Because of its complex structures and properties, dyes cannot be biodegraded and even harmful to the environment [3–8]. Consequently, before the wastewater discharges into the river, the excessive dyes have to be strictly treated. Many techniques have been developed to purify the dye-containing wastewater, such as adsorption [9–12], chemical coagulation [13], membrane separation [14,15],

ion exchange [16], photo-catalytic degradation [5,16,17], biological degradation [18], and some optimized combination processes [19,20].

Adsorption is a useful and interesting process because of its low cost, high removal rate, versatility, and easy synthesis [21]. The exploitation of novel and more effective adsorbents is always an important focus in related fields. Amorphous carbon materials, with their low cost, environmental friendliness, high surface area, feasible pore characteristics, and chemical-physical characteristics, have become potential adsorbents for the removal of contaminants from industrial wastewater [22]. The preparation of amorphous carbon materials from biomass materials has attracted increasing attention due to their high efficiency, minimization of chemical sludge, low operating cost, and raw material cost [23–25].

Photocatalytic degradation is also a promising method for the removal of organic pollutants due to the utilization of natural solar energy and features such as nontoxicity, safety, low energy consumption, reusability, high stability, and catalytic activity [5,17,26–28]. Semiconductor photocatalysts are the key to photocatalysis. Bismuth ferrate (BiFeO_3) is an inexpensive, stable, highly active, and environmental-friendly semiconductor photocatalyst with a narrow band gap of 2.0–2.7 eV [29,30]. Quite a few works have revealed that BiFeO_3 is an effective photocatalyst for the degradation of organic compounds [29–32]. The combination of adsorption and photocatalysis performs a synergistic action, not only will the dyeing wastewater be purified with more efficiency, the adsorbents can be recycled through the photocatalytic degradation of the adsorbed dyes [20,33]. Thus the method shows promise in resource utilization, economic benefit, and environmental protection.

Based on the above considerations, a nanocomposite of amorphous carbon fiber incorporated with BiFeO_3 (BiFeO_3 /carbon fiber) was developed in this work. Herein, the amorphous carbon fibers were prepared by the carbonization of cotton-linen fiber cloth, which was a biomass material, and the nanocomposite was prepared by the template method [34] and through optimizing the preparation process. The adsorptivity of the amorphous carbon fibers and the photocatalytic activity of the BiFeO_3 were combined in the developed BiFeO_3 /carbon fiber nanocomposite, its performance in removing the organic dyes from water and photocatalytic regeneration were studied. Methylene blue (MB) is a typical organic dye widely used in many industrial fields [35] and is highly toxic and very difficult to degrade [36]. Consequently, in this work, MB was selected as a representative dye to be used in studying the performance of the BiFeO_3 /carbon fiber nanocomposite. Material characteristics, MB adsorption properties and their dependence on a variety of parameters, adsorption isotherm and kinetic characteristics, as well as the photocatalytic regeneration effect were investigated for the BiFeO_3 /carbon fiber nanocomposite. The investigation results indicated that the BiFeO_3 /carbon fiber nanocomposite, as an adsorbent material, could efficiently remove the MB from the aqueous solution and the adsorption performance was not easily influenced by the solution environment. The adsorption capacity could be reproduced by photocatalytic regeneration and could be stable after repeating the adsorption-regeneration process cycle. The high efficiency, great stability, extensive and economic applicability, easy production, and recycling of the developed nanocomposite adsorbent are the highlight of the present work.

2. Results and Discussion

2.1. Characterisation of the Adsorbent Materials

In our manuscript, CT is the cotton-linen fiber cloth. CCT is the sample of the carbonized product of the cotton-linen fiber cloth. CT-BFO is the sample of BiFeO_3 that the cotton-linen fiber cloth was immersed in and heated at 850 °C. CCT-BFO is a sample of BiFeO_3 that the carbonized product of the cotton-linen fiber cloth was immersed in and heated. The X-ray diffraction (XRD) analysis method was employed to investigate the prepared CCT, CCT-BFO, and CT-BFO, as shown in Figure 1. The XRD pattern of the CCT shows only two wide peaks around 25° and 45°, which should correspond to the structure of amorphous carbon [37,38]. The XRD patterns of CT-BFO and CCT-BFO also indicate two wide peaks of amorphous carbon in similar positions as that of the CCT, but the other peaks that

can be assigned to the crystal planes of (100), (110), (1-10), (1-11), (200), (2-11), and (310) of BiFeO_3 are given in CCT-BFO (JCPDS no. 72-2122). Some peaks of BiFeO_3 can also be found in CT-BFO, but the intensity of these peaks is not strong. It is known from the XRD patterns that the CCT is an amorphous carbon material without BiFeO_3 contained in it; the CCT-BFO and CT-BFO are the composites of BiFeO_3 and amorphous carbon material, but the BiFeO_3 in CT-BFO demonstrates less crystallinity. As described in the “experiment procedures”, the preparation processes of the CCT, CCT-BFO, and CT-BFO all underwent the thermal annealing stages, therefore the amorphous carbon material contained in them should be generated by the carbonization of the cotton-linen fiber cloth material. No BiFeO_3 precursor was added during the preparation process of CCT, and thus it was only the amorphous carbon material, without the BiFeO_3 contained in it. The preparation process of CCT-BFO underwent two stages of thermal annealing. After the first annealing stage, which completed the carbonization of the cotton-linen fiber cloth material, the obtained CCT was immersed in BiFeO_3 precursor solution. After it adsorbed enough of the BiFeO_3 precursor, then the second annealing stage completed the calcination of BiFeO_3 precursor and generated the BiFeO_3 product. Thus, the obtained CCT-BFO was a composite of BiFeO_3 and amorphous carbon material. In the preparation process of CT-BFO, the cotton-linen fiber cloth material first adsorbed enough of the BiFeO_3 precursor during its immersion in the BiFeO_3 precursor solution. Then, the annealing process of the cotton-linen fiber cloth material containing the BiFeO_3 precursor completed the carbonization and calcination simultaneously. As a result, the CT-BFO was also a composite of BiFeO_3 and amorphous carbon material. Since the carbonization and calcination proceeded simultaneously, the impurities caused by the pyrolysis of the cotton-linen fibers might be mixed into the BiFeO_3 , resulting in the demonstration of less crystallinity of BiFeO_3 . We performed the Raman spectra on three samples as shown in the Figure S1 (Supplementary Materials). The intensities of the D peak and the G peak were different for the three samples. The ratios of D/G were calculated from the changes in the intensities of the D and G peaks, which are marked in Figure S1. It can be seen from the figure that most of the carbon contained in the material exists as amorphous carbon, and the surface chemical states indeed were not the reason for the adsorption property differences [39].

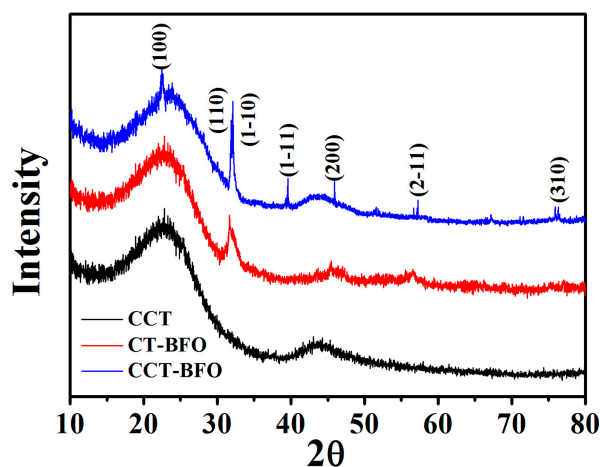


Figure 1. X-ray diffraction (XRD) patterns of the CCT, CT-BFO, CCT-BFO respective.

The scanning electron microscope (SEM) images of the prepared CCT, CT-BFO and CCT-BFO are shown in Figure 2. The figure demonstrates that the amorphous carbon materials, which are the component parts of the three samples, are fiber-shaped. Figure 2a,c,e demonstrate that the well dispersed carbon fibers had high length-to-diameter ratios and lengths from several tens of micrometers to several hundreds of micrometers. Figure 2b,d,f, which are the magnified SEM images, demonstrate that the diameters of the carbon fibers are from four to ten micrometers. It must be known from the fracture parts of the carbon fibers, as shown in Figure 2b,d,f, that the carbon fibers had a

hollow structure with the hollow diameters being about several micrometers. And it can be seen that there are some pores on the CT-BFO and CCT-BFO samples that show a large surface area compared with the CCT one. These pores may be from the immersion of the acidic aqueous BFO precursor etching the fiber to form pores. In addition, the CCT-BFO sample shows smaller BFO nanoparticles on the amorphous carbon fiber, leading to larger surface area. The acid etching and size of the BFO nanoparticles can affect the surface area, resulting in a different adsorption property. The SEM images revealed that the amorphous carbon materials generated by the carbonization of the cotton-linen fiber cloth material replicated the shape and structure of the cotton-linen fibers, and thus it can be a good carrier material for the particle materials.

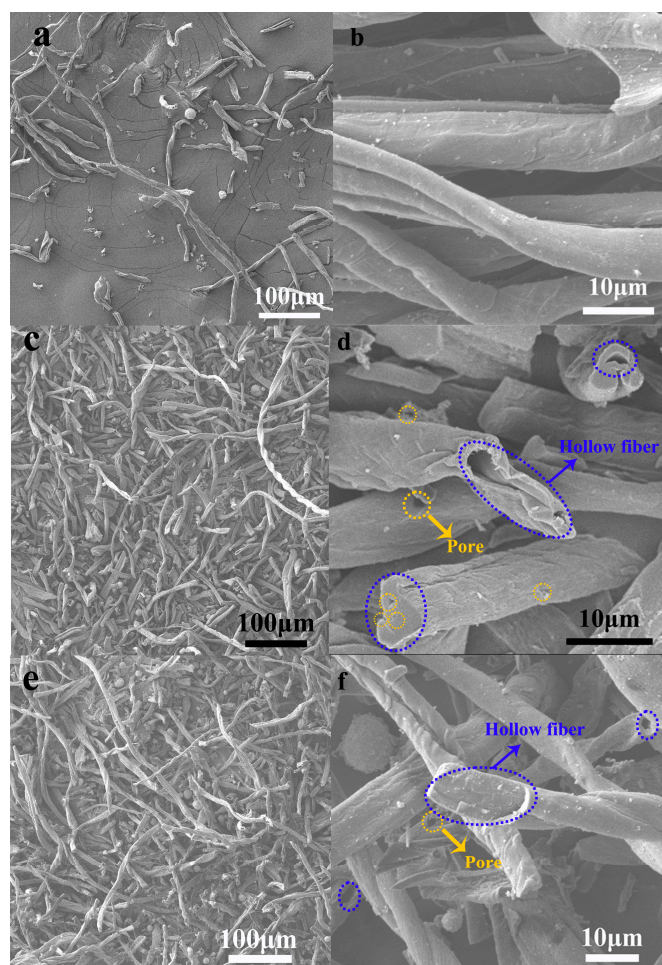


Figure 2. The scanning electron microscope (SEM) images of CCT (a,b); CCT-BFO (c,d) and CT-BFO (e,f) respective.

The transmission electron microscopy (TEM) images of CCT, CT-BFO and CCT-BFO are respectively shown in Figure 3a–c. Figure 3a indicates that the component materials of CCT are pure hollow-structured carbon fibers without BiFeO_3 material incorporated to them. Figure 3b shows that the carbon fibers in CT-BFO are coated by BiFeO_3 particles, and the BiFeO_3 particles coated on the surfaces of carbon fibers are badly dispersed and seriously aggregated. Figure 3c shows that the carbon fibers in CCT-BFO are also coated by BiFeO_3 particles, but the BiFeO_3 particles are well dispersed and uniformly coated on the surfaces of the carbon fibers. The difference of the states of the BiFeO_3 particles coated on carbon fibers between the CT-BFO sample and CCT-BFO sample should be ascribed to the different preparation processes of the two samples. CCT-BFO underwent two stages of annealing while CT-BFO was annealed once. The bad dispersivity of the BiFeO_3 particles coated on the

carbon fibers in the CT-BFO sample should be caused by the mutual interference of the concurrent carbonization and calcination processes.

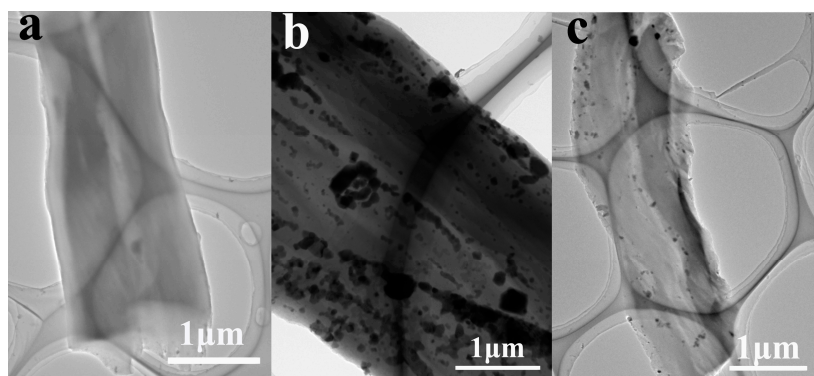


Figure 3. The transmission electron microscopy (TEM) images of CCT (a); CT-BFO (b); and CCT-BFO (c) respective.

The high resolution transmission electron microscopy (HRTEM) images of the CCT-BFO obtained by the magnification of the TEM observations (Figure 4a,b) are shown in Figure 4c,d. It is indicated from the HRTEM images that the BiFeO_3 particles coated on carbon fibers had nanosized diameters of about 5 nm. The compact interface between the BiFeO_3 nanoparticle and the outer-shell of the carbon fiber demonstrated in Figure 4c reveals that the jointing between the BiFeO_3 nanoparticles and the carbon fibers was firm. Figure 4c,d also clearly demonstrate the (200) and (110) crystal planes of the BiFeO_3 nanoparticles and the uniform orientations of the lattice fringes reveal that the BiFeO_3 nanoparticles coated on carbon fibers might be a single crystal structure.

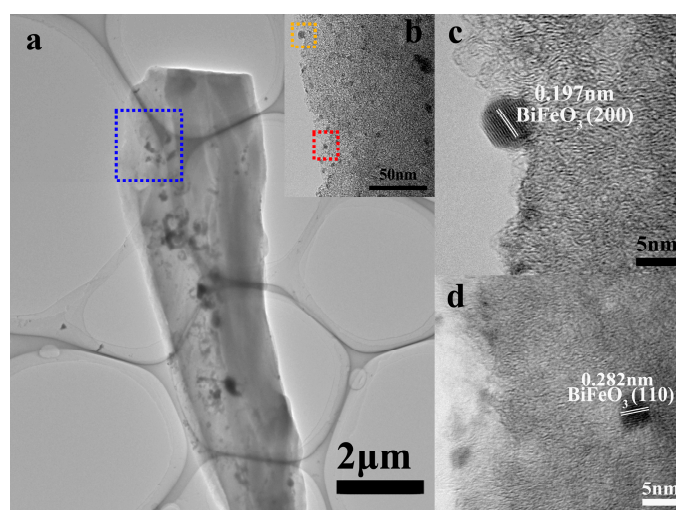


Figure 4. The TEM image (a,b) and high resolution transmission electron microscopy(HRTEM) images (c,d) of the CCT-BFO. The blue square in (a) is (b), and the orange and red square in (b) are corresponds to HRTEM images (c,d).

From the measurements of XRD, SEM, TEM, and HRTEM, it can be known that the component materials of the CCT are amorphous structured carbon fibers, the CT-BFO is a composite whose component materials are the amorphous structured carbon fibers coated by BiFeO_3 particles, and the CCT-BFO is a nanocomposite whose component materials are the amorphous structured carbon fibers coated by BiFeO_3 nanoparticles.

Nitrogen adsorption and desorption experiments were performed on the samples to measure the BET specific surface areas and the pore diameter distributions of the CCT-BFO, CT-BFO, and CCT, respectively. The data curves of the adsorption/desorption cycles are shown in Figure 5. The inset diagram of Figure 5 shows the pore diameter distributions of the three samples. The surface area of the sample can be calculated by the BET method from the data in Figure 5a, and the pore size distribution can be calculated by the BJH method from the data in Figure 5b (inset in Figure 5a). The calculated BET specific surface areas and the Barrett–Joyner–Halenda (B.J.H) pore distribution volume ratios of the micropores of the three samples from the measured data of nitrogen adsorption/desorption cycles are listed in Table 1.

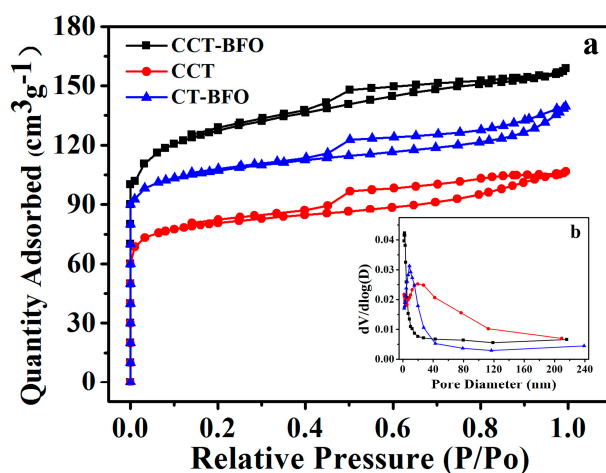


Figure 5. (a) Nitrogen adsorption/desorption isotherms of CCT-BFO, CT-BFO, and CCT respective and (b) the pore size distribution of three samples.

Table 1. The specific surface area and the micropores volume ratio of the CCT-BFO, CT-BFO, and CCT, respectively.

Samples	CCT-BFO	CT-BFO	CCT
BET specific surface area (m ² /g)	442.55	350.04	278.27
Volume ratio of micropores (<2 nm) (%)	8.63	15.21	18.46

As shown in Table 1, the specific surface area of the CCT-BFO is much larger than those of the CT-BFO and CCT, while the volume ratio of the micropores of the CCT-BFO is the lowest in the three samples. This should be ascribed to the fact that the preparation of CCT-BFO underwent two stages of thermal annealing; the preparation processes of the CCT and CT-BFO both underwent only one stage of thermal annealing and the immersion of the aqueous acidic BFO precursor to etching the fiber to form pores. Two annealing stages could create more surface ablations of the carbon fibers, which thinned the shells of the carbon fibers, enhanced the surface roughness, and the dispersivity of carbon fibers. More surface ablations also caused more fractures of the carbon fibers, resulting in more hollow structures (with micrometer sized diameters) being exposed, and thus more inner surfaces being accessible. Therefore, compared to the CCT and CT-BFO, the CCT-BFO had a higher specific surface area and a lower volume ratio of micropores.

2.2. The Performances of MB Adsorption of the Adsorbents

The measured absorbencies of the MB aqueous solutions with an initial concentration of 10 mg·L⁻¹ and pH value of 7, added by pure BiFeO₃, CCT, CCT-BFO, and CT-BFO, respectively, at different times are shown in Figure 6. This indicates that the peak absorbencies of the MB aqueous solutions decrease with time increasing due to the removal of MB by the adsorption effects of the adsorbents.

The decrease in peak absorbency of the MB aqueous solutions added by the pure BiFeO₃ was less than 10% after 150 min, which is obviously lower compared to the other three MB aqueous solutions added by the CCT, CCT-BFO, and CT-BFO, respectively. Thus, this indicates that the adsorption ability of the pure BiFeO₃ is poor. Therefore, we do not further consider the pure BiFeO₃ in this study and also do not consider the influence of the loading amount of BiFeO₃.

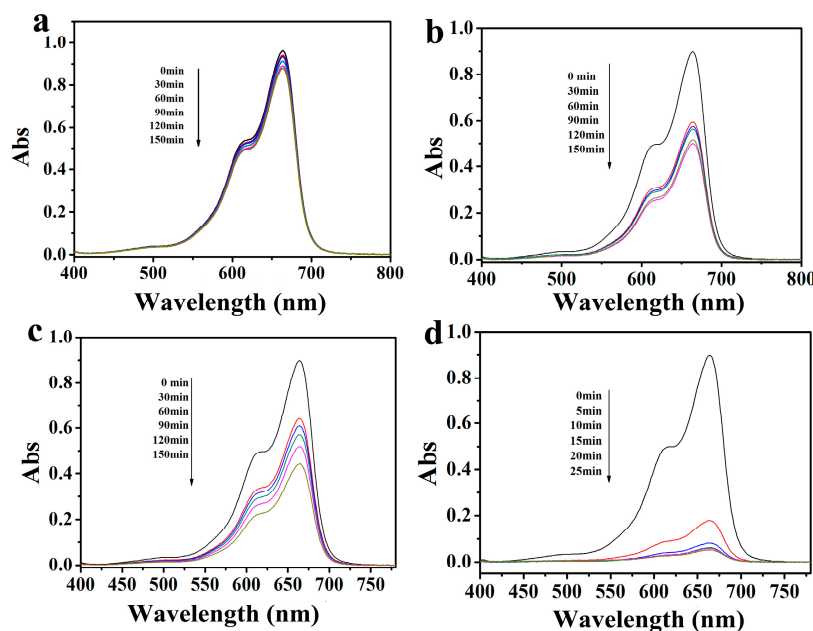


Figure 6. Changes to the absorbencies of the MB aqueous solutions, added by different adsorbent, in dependence of time. (a) added by pure BiFeO₃; (b) added by CCT adsorbent; (c) added by CCT-BFO adsorbent; and (d) added by CT-BFO adsorbent. The MB initial concentration is 10 mg·L⁻¹, the pH value of the solutions is 7.

Figure 6 demonstrates that the CCT-BFO adsorbent demonstrated the best adsorption effect in the three amorphous carbon contained adsorbents because the peak absorbency of the MB aqueous solution added by the CCT-BFO dropped to near 0 within 25 min, while the peak absorbencies of the MB aqueous solutions added by CCT or CT-BFO dropped to only about half of the initial values within 150 min. The adsorption performance of the adsorbent has a considerable relationship with its specific surface area and pore size distribution [40,41]. Among the three adsorbents of CCT-BFO, CT-BFO, and CCT, the CCT-BFO had the highest specific surface area and the lowest volume ratio of micropores, which are unavailable for molecular adsorption [42,43], thus it could have the best adsorption performance.

The change in MB concentration during the adsorption process can be calculated from the absorbency of the MB aqueous solution. Because the dye concentration is basically directly proportional to the absorbency in the low concentration range [5], the relative concentration and the removal ratio of the MB at any time during the adsorption process can be calculated by the following equations:

$$C/C_0 = A/A_0, \quad (1)$$

$$\eta = [(C_0 - C)/C_0] \times 100\% = [(A_0 - A)/A_0] \times 100\% \quad (2)$$

where C/C_0 is the MB relative concentration, C_0 is the MB initial concentration, C is the MB concentration at a certain time, η is the removal ratio of MB, A_0 is the initial peak absorbency, and A is the peak absorbency at a certain time.

The adsorption capacity Q_t (mg g^{-1}) of the adsorbent is calculated according to the following equation:

$$Q_t = (C_0 - C)V/m, \quad (3)$$

where V is the volume of the solution (L), and m is the mass of dry adsorbent (g).

By calculating the data of Figure 6, the obtained data diagram of time-varying relative concentrations of the MB aqueous solutions, added by the adsorbents of CCT-BFO, CT-BFO, and CCT respectively, is shown in Figure 7a. Figure 7a indicates that the MB relative concentrations of the MB aqueous solutions, respectively added by the CCT adsorbent and CT-BFO adsorbent, dropped to 57.46% and 49.22%, respectively, after 150 min of the adsorption process, meaning a MB removal ratio of 42.54% and 50.78%, respectively. However, for the MB aqueous solution, which was added by the CCT-BFO adsorbent, the MB relative concentration dropped to 5.79% after only 25 min of adsorption process, meaning a MB removal ratio of 94.21%, which nearly removed the MB. The time-varying adsorption capacities of the three adsorbents calculated from the data of Figure 7a, are shown in Figure 7b. Figure 7b indicates that the adsorption capacity of CCT-BFO was higher than those of the CCT and CT-BFO, though they all gradually increased with time due to the amount of adsorbed MB molecules gradually increasing as the adsorption progressed. The MB relative concentrations and the adsorption capacities of the adsorbents will tend to be stable as the adsorption equilibriums are approached. Figure 7 demonstrates that the CCT-BFO added MB aqueous solution reached the adsorption equilibrium within 25 min, which is much more rapid compared to the CCT added MB aqueous solution and the CT-BFO added MB aqueous solution. These results indicate that the CCT-BFO could remove MB with much more efficiency relative to CCT and CT-BFO. Therefore, the following further study was focused on the CCT-BFO and the CCT-BFO added MB aqueous solutions.

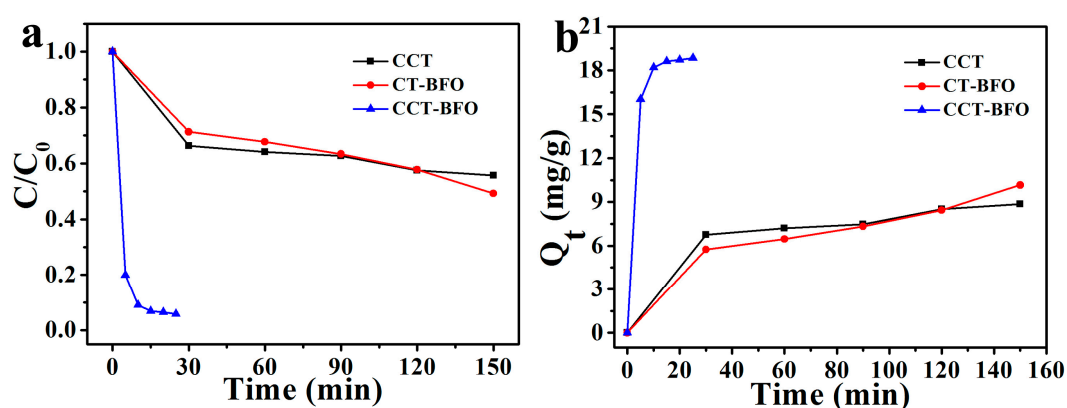


Figure 7. (a) Changes of the relative concentrations of MB aqueous solutions, added by different adsorbents, versus time; (b) Changes of the adsorption capacities of three adsorbents versus time.

2.3. Adsorption Isotherm Study

The adsorption characteristics and equilibrium parameters of several adsorption isotherm models indicate the interaction between the adsorbent and the adsorbate, and give comprehensive information on the nature of the interaction. The monolayer adsorption on energetically uniform adsorbent sites is predicted by Langmuir isotherm [44]. The equation can be expressed as [45]:

$$Q_e = (Q_m k_L C_e) / (1 + k_L C_e), \quad (4)$$

where C_e is the equilibrium concentration of the dyes solutions ($\text{mg}\cdot\text{L}^{-1}$), Q_e is the adsorption capacity at equilibrium ($\text{mg}\cdot\text{g}^{-1}$), k_L is the constant related to free energy of adsorption ($\text{L}\cdot\text{mg}^{-1}$), and Q_m is the maximum adsorption capacity at monolayer coverage ($\text{mg}\cdot\text{g}^{-1}$). Plotting C_e/Q_e against C_e gives a straight line, and the Q_m , k_L can be calculated from the slope and intercept.

The Freundlich model can be used to represent the adsorption at a heterogeneous surface, the equation of the Freundlich model can be expressed as [46]:

$$\ln Q_e = \ln k_F + (\ln C_e)/n, \quad (5)$$

where k_F ($L \cdot mg^{-1}$) is a Freundlich constant related to the adsorption capacity, and n is the heterogeneity factor. Plotting $\ln Q_e$ against $\ln C_e$ gives a straight line, and the k_F , n can be calculated from the intercept and slope.

Figure 8 shows Langmuir adsorption isotherm and Freundlich adsorption isotherm for the MB adsorption by CCT-BFO adsorbent. Table 2 lists some key parameters calculated from Langmuir model and Freundlich model. Figure 8 and Table 2 indicate that the experiment data are well fit in the Langmuir model and Freundlich model. The determination coefficients (R^2) obtained from the Langmuir model and Freundlich model are all above 0.99, but the R^2 obtained from Freundlich model (0.9937) is a little higher than that obtained from the Langmuir model (0.9925). This suggests that the adsorption of the MB molecules on CCT-BFO surfaces were mainly homogeneous adsorption because of the uniform distribution of the active adsorption sites on the carbon fibers' surfaces of CCT-BFO. A little adsorption of the heterogeneous surface also existed due to the electrostatic attraction between the slight negative charge that existed on $BiFeO_3$ nanoparticles' surfaces and the MB cations. The large values of k_F and n indicate that the adsorption of MB on CCT-BFO was advantageous.

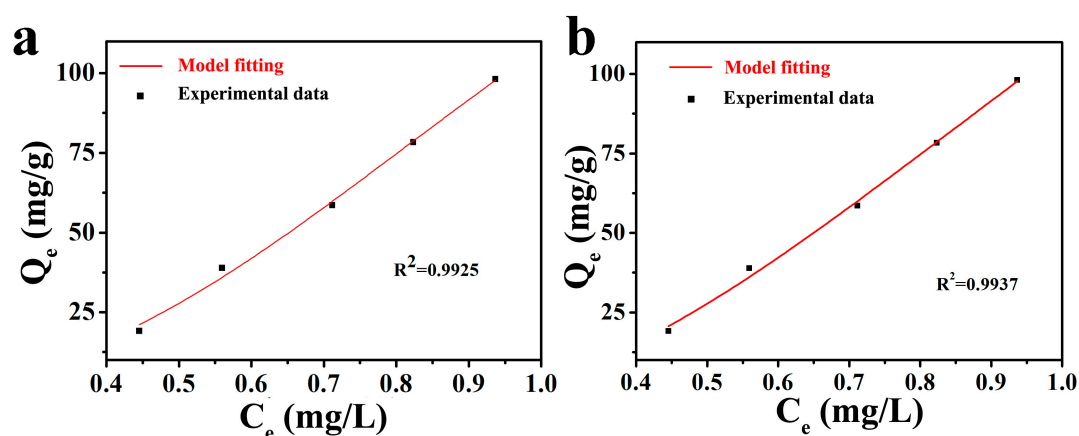


Figure 8. Langmuir isotherm model (a) and Freundlich isotherm model (b) for the MB adsorption by CCT-BFO. The pH values of the MB aqueous solutions are 7.

Table 2. Parameters, for the adsorption of MB onto CCT-BFO, of the Freundlich and Langmuir isotherm models.

Dye	Langmuir			Freundlich			
	Q_{max} (mg/g)	k_L (L/mg)	R^2	R_L	k_F (L/mg)	n	R^2
MB	98.1264	0.8001	0.9925	0.1111	7.9641	0.4669	0.9937

Furthermore, the essential characteristics of the Langmuir isotherm parameters can be expressed in terms of a dimensionless constant called the separation factor, and it can be expressed by equation [47]:

$$R_L = 1/(1 + k_L C_0), \quad (6)$$

Previous studies have shown that the adsorption is unfavorable ($R_L > 1$), favorable ($R_L < 1$), linear ($R_L = 1$), or irreversible ($R_L = 0$) [48]. The R_L value is showed in Table 2, and its between 0 and 1, which indicates a gainful process of the adsorption of MB onto the CCT-BFO.

In the Langmuir model, the maximum adsorption capacity (Q_{\max}) of the CCT-BFO was calculated, the value is 98.1246 mg/g, and as listed in Table 2. The comparisons of Q_{\max} of the CCT-BFO and other reported adsorbents for MB are listed in Table 3. In this table, the adsorption capacity for MB of CCT-BFO is higher than many other adsorbents prepared by different methods.

Table 3. The maximum adsorption capacity of various adsorbents for MB.

Adsorbent	S_{BET} , m^2/g	Q_{\max} , mg/g	Source
Charred citrus fruit peel	526	25.5	Dutta et al. [49]
Palygorskite/carbon	46.45	37.79	Xue-ping Wu, et al. [50]
UiO-66	981	24.5	Ji-Min Yang [51]
$\text{Fe}_3\text{O}_4/\text{Zn-Al-LDH}$	133	36.9	Liang-guo Yan, et al. [52]
FSAC	1867	52.63	F. Marrakchi, et al. [53]
CCT-BFO	442.55	98.12	This Work

2.4. Adsorption Kinetics Study

In common, adsorption kinetics are generally used to predict the adsorption rate and explain the controlling mechanism of the adsorption process. Because there is no ideal single-factor condition in reality, the model needs to be revised. Pseudo-first-order and pseudo-second-order models are investigated to describe the behavior of MB adsorption onto CCT-BFO.

Pseudo-first order model can usually be expressed as [54]:

$$\ln(Q_e - Q_t) = \ln Q_e - k_1 t, \quad (7)$$

where Q_e and Q_t ($\text{mg} \cdot \text{g}^{-1}$) are the adsorption capacities of adsorbent at equilibrium and at a given time t , respectively, k_1 is the rate constant of the pseudo-first-order adsorption (min^{-1}). Using this equation, the values of k_1 and Q_e were calculated from the slope and intercept of the plot of $\ln(Q_e - Q_t)$ versus t , respectively (see Figure 9a).

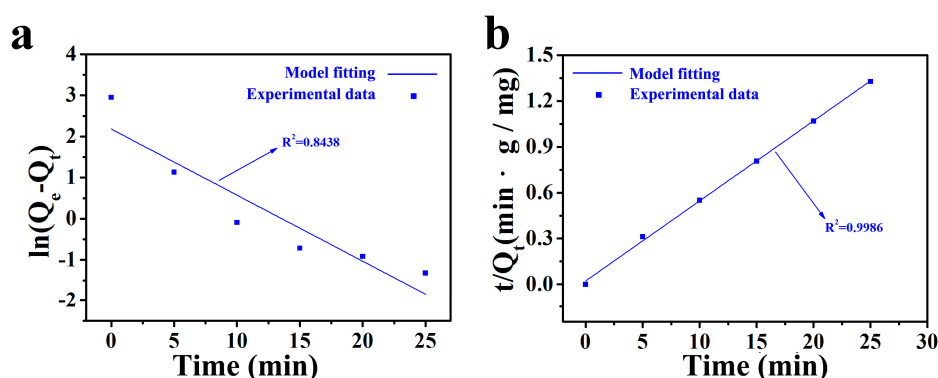


Figure 9. Pseudo-first order adsorption kinetics (a) and pseudo-second order kinetics (b) for the MB adsorption by CCT-BFO. The pH values of the MB aqueous solutions are 7.

The pseudo second-order adsorption kinetics model can usually be expressed as [55]:

$$t/Q_t = 1/k_2 Q_e^2 + t/Q_e, \quad (8)$$

where k_2 is the equilibrium rate constant of pseudo-second-order adsorption ($\text{g} \cdot \text{mg}^{-1} \cdot \text{min}^{-1}$). The slope and intercept of the plot of t/Q_t versus t were used to calculate the second-order rate constant (k_2) and the adsorption capacity of the adsorbent at equilibrium (Q_e) (see Figure 9b).

The two kinetic models were drawn with the key parameters, which are listed in Table 4, and the fitted plots are shown in Figure 9a,b. Figure 9 demonstrates that, through model fitting

of the experimental data, a poor correlation is observed for the pseudo-first-order model and the determination coefficient (R^2) was less than 0.90. Therefore, it can be concluded that the process of adsorption does not effectively follow the pseudo first order kinetics. The experimental data are more in line with the prediction of the pseudo-second-order model. The determination coefficient ($R^2 > 0.998$) obtained from the pseudo-second-order model is higher than that of the pseudo-first-order model, as listed in Table 4. Furthermore, for the pseudo-second-order model, the values of adsorption capacity at equilibrium are more consistent between the experimental value ($Q_{e,exp}$, 19.109 mg/g) and the calculated value ($Q_{e,cal}$, 18.704 mg/g). Thence, the pseudo-second-order model is more suitable with the experimental data.

Table 4. Parameters of the pseudo-first-order model and pseudo-second-order model for the adsorption of MB onto CCT-BFO.

Equations	$Q_{e,exp}$ (mg/g)	Pseudo-First-Order Equation $\ln(Q_e - Q_t) = \ln Q_e - k_1 t$			Pseudo-Second-Order Equation $t/Q_t = 1/k_2 Q_e^2 + t/Q_e$		
		k_1 (min^{-1})	$Q_{e,cal}$ (mg/g)	R^2	$k_2 \times 10^2$ ($\text{g}/(\text{mg} \cdot \text{min})$)	$Q_{e,cal}$ (mg/g)	R^2
MB	19.109	0.364	19.981	0.8438	5.417	18.704	0.9986

2.5. Effect of Initial Solution pH

In the process of adsorption, the pH value of the solution has an important influence, because of the features that work on the adsorbent surface and can change the protonation of the functional groups. Therefore, the pH values were changed from 1.0 to 14.0, and the results of the adsorption experiments are shown in Figure 10. It can be seen from the figure that the removal ratio of MB and the adsorption capacity of CCT-BFO were not obviously influenced by the change of initial pH value of the MB aqueous solution. The reason should be that the oxygen-containing groups on the surfaces of the carbon fibers of CCT-BFO were almost completely decomposed during the annealing stage of the preparation process [56]. The protonation and deprotonation of the functional groups, determined by the pH value, did not exist on the carbon fibers' surfaces [57] and thus the electrostatic attraction effect between the carbon fibers' surfaces and the MB ions could not be obviously changed by a different pH value. This result revealed that the adsorption performance of the CCT-BFO is relatively stable and not easily influenced by the environmental conditions.

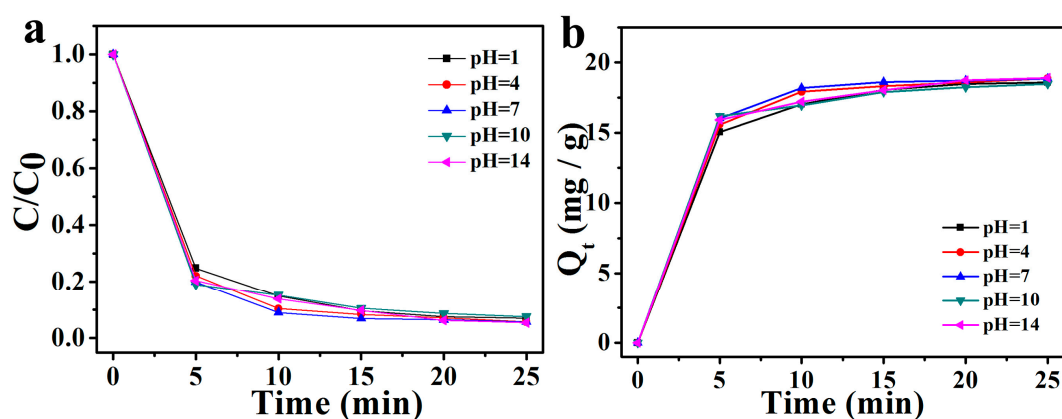


Figure 10. (a) Changes of the relative concentrations of MB aqueous solutions, added by the CCT-BFO adsorbent, versus time under different initial pH values; (b) Changes of the adsorption capacities of the CCT-BFO adsorbent versus time under different pH values. The MB initial concentration is $10 \text{ mg} \cdot \text{L}^{-1}$.

2.6. Regeneration of the Adsorbent by Photocatalysis

Many traditional adsorbents cannot continue to adsorb the adsorbates after adsorption operations and can only be discarded, resulting in the waste of resources and the generation of new contaminants. It is a very important factor for the regeneration and reuse of adsorbents in economy and industrial productive cost. In this work, the photocatalysis method was used to regenerate the adsorbent.

The FTIR spectra of the as prepared CCT-BFO, the CCT-BFO after 30 min of MB adsorption (which had already reached adsorption equilibrium, as demonstrated in Figure 7), and the photocatalysis regenerated CCT-BFO, which was obtained by irradiating the CCT-BFO for 30 min by the 300 W xenon lamp after MB adsorption, are shown in Figure 11. By comparing Figure 11a,b, it can be seen that several distinct peaks appeared after the adsorption of the MB molecules on the adsorbent. The peak at 1589 cm^{-1} reflects the stretching vibration band of C-N bond in the benzene ring [58]. The peak at 1383 cm^{-1} reflects the rocking vibration of the C-H bond [58]. The peak at 1324 cm^{-1} corresponds to the C-N bending vibration of the N atom attached to the benzene ring [59]. The peak at 1040 cm^{-1} corresponds to the stretching vibration of the C-S bond [59]. The peak at 884 cm^{-1} is associated with the rocking vibration of the phenyl ring skeleton plane [59]. It can be proved that these peaks appeared after adsorption and belong to the characteristic peaks of MB molecules. Figure 11c demonstrates that the characteristic peaks of the MB molecules disappeared after photocatalytic regeneration, and the FTIR spectrum of the photocatalysis regenerated CCT-BFO is basically identical to that of the as prepared CCT-BFO, which can prove that the MB molecules adsorbed on the CCT-BFO were removed after photocatalysis regeneration.

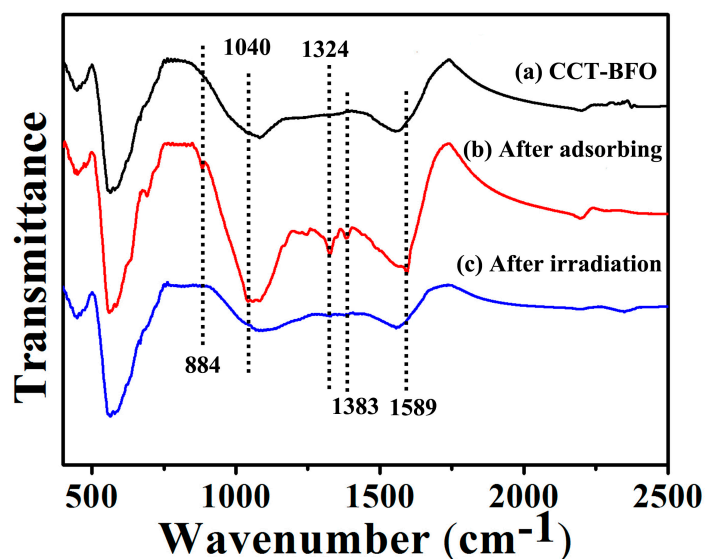


Figure 11. Fourier-transform infrared (FTIR) spectra of (a) the as prepared CCT-BFO; (b) the CCT-BFO after MB adsorption; and (c) the CCT-BFO after being regenerated by photocatalysis.

The mechanism of photocatalytic regeneration of CCT-BFO is illustrated in Figure 12. Upon the irradiation, electron-hole pairs were generated in BiFeO_3 nanoparticles, the photogenerated holes and electrons moved in the valence and conduction bands, respectively, and then reacted with the water molecules, and dissolved the oxygen molecules and hydrogen ions, etc., at the surfaces of the BiFeO_3 nanoparticles to generate the hydroxyl radicals and hydrogen peroxide, etc., which are reactive molecules possessing a high activity of oxidizing organic dyes [60]. The hydrogen peroxide and hydroxyl radicals further oxidized the adsorbed MB molecules to finally generate water and carbon

dioxides, hence the adsorbent was regenerated and could be reused for adsorption. The photocatalytic degradation process of MB is as follows [60]:

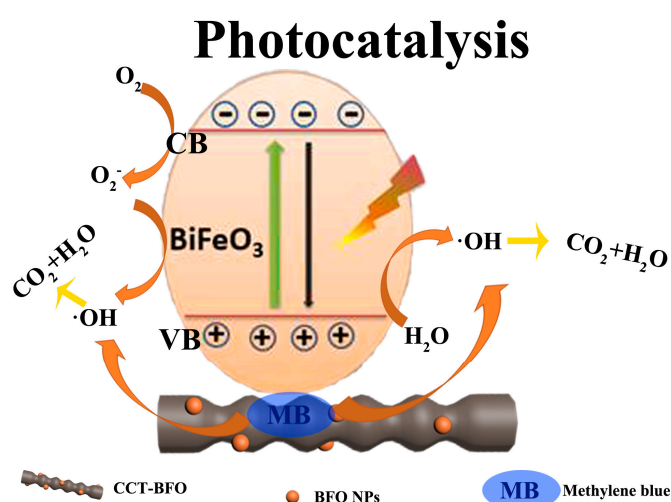
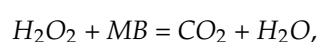
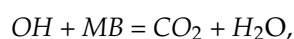
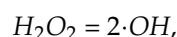
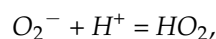
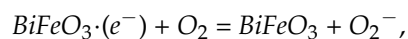
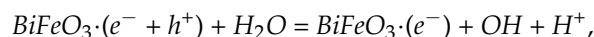


Figure 12. The schematic about the mechanism of regeneration of CCT-BFO through photocatalytic degrading MB molecules by light-irradiating the BiFeO₃ nanoparticles coated on carbon fibers' surfaces.

In addition, the nanometer sizes of the BiFeO₃ nanoparticles are beneficial for the high efficiency of the disassociation of the photogenerated holes and electrons, while the conductance character of the carbon fibers, which act as the carriers of the BiFeO₃ nanoparticles, could effectively inhibit the recombination of the photogenerated holes and electrons [5]. These two factors could help to enhance the efficiency of the photocatalytic degradation of the adsorbed dyes, and hence could help to enhance the rate of the photocatalytic regeneration of the adsorbent.

After the photocatalytic regeneration, the reproducibility becomes another important factor that can evaluate the performance of the adsorbent material. Whether the performance of the adsorbent changes after repeated treatments of adsorption-photocatalytic regeneration signifies whether the adsorbent can be recycled. Experimental results indicated that the CCT-BFO adsorbent could reproduce the performance of adsorbing MB after the photocatalytic regeneration treatments, the required time for reaching the equilibrium adsorption decreased as the processing time of the photocatalytic regeneration increased, but it did not continue to decrease when the processing time of the photocatalytic regeneration was above 30 min, as shown in Figure 13a. The result indicates that the adsorption performance of the CCT-BFO adsorbent can be further reproduced after 30 min of a photocatalytic regeneration treatment. Thus, the processing time of the photocatalytic regeneration in every cycle of adsorption-photocatalytic regeneration was 30 min. The data diagram of time-varying

relative concentrations of the MB aqueous solutions, added by CCT-BFO undergoing a different number cycles of adsorption-photocatalytic regeneration, is shown in Figure 13b. It can be judged from the figure that the adsorption capacity of CCT-BFO adsorbent remained basically stable after five cycles of adsorption-photocatalytic regeneration. The calculated final MB removal ratio from Figure 13b changed from 94.21% to 91.98% after five cycles of adsorption-photocatalytic regeneration. The difference is less than 3%. Therefore, it is a cost-effective, function-effective, and stable way for the removing of dyes by using the CCT-BFO as an adsorbent.

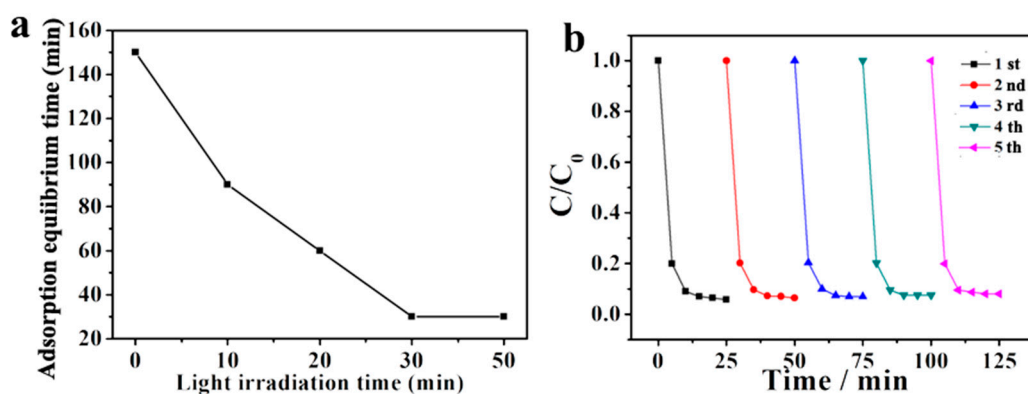


Figure 13. (a) Correlation between the time duration for reaching the equilibrium adsorption and the time duration of light-irradiating the CCT-BFO adsorbent after equilibrium adsorption of MB; (b) Changes in the relative concentrations of MB aqueous solutions, added by the CCT-BFO adsorbents undergoing a different number of cycles of adsorption-photocatalytic regeneration, versus time. The MB initial concentration is $10 \text{ mg}\cdot\text{L}^{-1}$, the pH value of the solution is 7.

3. Experiment Procedures

3.1. Materials

Bismuth nitrate ($\text{Bi}(\text{NO}_3)_3\cdot 5\text{H}_2\text{O}$), Iron nitrate ($\text{Fe}(\text{NO}_3)_3\cdot 9\text{H}_2\text{O}$) and ethanol were purchased from Tianli Chemical Reagent Co., Ltd. (Tianjin, China). MB with the purity of above 98% was purchased from Shanghai Yiji Industrial Co., Ltd. (Shanghai, China). The cotton-linen fiber cloth (CT) was from Shanghai Wangwang Textile Co., Ltd. (Shanghai, China). Nitric acid (HNO_3) was purchased from Xilong Chemical Reagent Co., Ltd. (Guangdong, China). All reagents were analytical reagent grade and used without further purification.

3.2. Preparation of BiFeO_3 /Carbon Fibre Composites

BiFeO_3 /Carbon fiber composites were prepared by the template method from cotton-linen fiber cloth and BiFeO_3 precursor. The cotton-linen fiber cloth was cut into small pieces. These pieces were washed with deionized water and ethanol five times, respectively, then dried at 80°C for 8 h to complete the cleaning treatment. The cleaned and treated pieces of cotton-linen fiber cloth were put in the middle of a horizontal furnace, and then heated at 850°C under nitrogen flow for 2 h to obtain the carbonized product of the cotton-linen fiber cloth material (CCT). 2.25g $\text{Bi}(\text{NO}_3)_3\cdot 5\text{H}_2\text{O}$ and 2.71 g $\text{Fe}(\text{NO}_3)_3\cdot 9\text{H}_2\text{O}$ (molar ratio of Bi and Fe was 1:1.2) were dissolved in 70 mL HNO_3 aqueous solution (10 wt %) at room temperature under constant stirring for 1 h until clear to obtain the BiFeO_3 precursor solution. CCT was immersed in a quantity of BiFeO_3 precursor solution for several minutes, then put in a horizontal furnace and heated at 800°C under nitrogen flow for 2 h to obtain one sample of BiFeO_3 /Carbon fiber composite(CCT-BFO). The cleaned and treated pieces of cotton-linen fiber cloth were immersed in a quantity of BiFeO_3 precursor solution for a few minutes, then put in a horizontal furnace and heated at 850°C under nitrogen flow for 2 h to obtain another sample of BiFeO_3 /Carbon

fiber composite (CT-BFO). A quantity of BiFeO₃ precursor solution was dried at 80 °C for 3 h, then put in a horizontal furnace and heated at 800 °C under nitrogen flow for 2 h to obtain the pure BiFeO₃.

3.3. Adsorption Experiments

Adsorption experiments were carried out in a glass flask containing 100 mL of MB aqueous solution with different concentrations that were prepared by proper dilution at room temperature (20 ± 3 °C). The solution pH (pH = 1, 4, 7, 10 and 14 respective) was adjusted by adding diluted HNO₃ or NaOH solution. 0.05 g of adsorbent (CCT-BFO, CT-BFO or CCT, which were ground to be powder state) was added into the MB aqueous solution, then the suspension mixture was magnetically stirred in dark. Microsamplings of the suspension were drawn every 5 min, and then centrifugated for 10 min to obtain the clear sample solutions. Their absorbencies were measured by a “UV-vis spectrophotometer (Model Shimadzu UV2550, Tokyo, Japan)” at the maximum absorptive wavelength of MB (664 nm), and used for determining the time-dependent change of the MB concentration.

3.4. The Experiment of Photocatalytic Regeneration of the Adsorbent

Photocatalytic regenerations of the adsorbent were performed at room temperature (20 ± 3 °C). After 30 min of MB adsorption in MB aqueous solution with the initial concentration of 10 mg·L⁻¹ and pH value of 7, the wet adsorbent was separated from the solution by centrifugation, then put in a glassware that was located 20 cm from the light source and irradiated by a 300 W xenon lamp for a period of time, which was the processing time of the photocatalytic regeneration treatment.

3.5. Material Characteristics

The XRD patterns of the adsorbent materials were characterized with a Bruker D8 Advance X-ray diffractometer equipped with a graphite monochromatized Cu K α radiation ($\gamma = 1.541874$ Å). The structures and morphologies of the adsorbent materials were characterized by transmission electron microscopy and high resolution transmission electron microscopy (TEM, HRTEM, JEOL-JEM2100, Tokyo, Japan), and field emission scanning electron microscopy (SEM, Hitachi S-4800, Hitachi High-Technologies Corporation, Tokyo, Japan). The surface functional groups of the adsorbent materials were determined by the Fourier-transform infrared (FTIR) spectra (Bruker Equinox 55 Spectrometer, Bruker Optics, Berlin, Germany). The specific area and the pore volume of the adsorbent materials were measured by the BET method and the B.J.H. method [61]. The employed apparatus was a Tristar II 3020 s.

4. Conclusions

In this work, a novel and efficient CCT-BFO nanocomposite adsorbent with superior adsorption capacity for the removal of dye is prepared by a template method and optimizing the preparation process. Through the carbonization-immersion-calcination procedure, the superior adsorption capacity of the amorphous carbon material and the photocatalytic property of BiFeO₃ were combined in the prepared CCT-BFO nanocomposite adsorbent, consequently MB could be photodegraded after being adsorbed, and thus achieve the regeneration of the adsorbent. The prepared CCT-BFO adsorbent was well structured and its specific surface characteristics are beneficial for the adsorption of contaminations. It removed most of the MB molecules from the aqueous solutions within several tens of minutes, and the adsorption performance is not easily influenced by the solution environments. The equilibrium adsorption isotherm revealed that the adsorption process could be well described by the classical models, and the maximum adsorption capacity of the MB onto the CCT-BFO was higher than many other reported adsorbents. The kinetic adsorption followed the pseudo-second-order kinetic model. Furthermore, the CCT-BFO could be effectively regenerated by the photocatalysis method due to the photocatalytic degradation of the organic compounds by the BiFeO₃ nanoparticles contained in it. The adsorption capacity of the CCT-BFO could be reproduced under light irradiation for several tens of minutes, and could be stable after five cycles of the adsorption-regeneration process. The investigation

proved that the CCT-BFO nanocomposite is an efficient, cost effective, and recyclable adsorbent for practical application in the treatment of dye wastewaters.

Supplementary Materials: The following are available online at <http://www.mdpi.com/2073-4344/8/7/267/s1>, Figure S1: The Raman spectra of the three samples.

Author Contributions: All the authors did the work of work design, experiment, and measurement, and discussed the writing of the manuscript. The manuscript was written through the contributions of all authors. All authors have given approval to the final version of the manuscript.

Funding: This research received no external funding.

Acknowledgments: This work was supported by the Chinese National Natural Science Foundation (Grant No. 61275117) and the Innovation Foundation of Key Laboratory of Functional Inorganic Material Chemistry, Ministry of Education of China. The authors thank Yang Qu for the academic communications, and the members of the Key Laboratory of Functional Inorganic Material Chemistry for technical support.

Conflicts of Interest: The authors declare no conflict of interest.

References

1. Tao, T.; Xin, K. A sustainable plan for China's drinking water. *Nature* **2014**, *511*, 527–528. [[CrossRef](#)] [[PubMed](#)]
2. Aksu, Z. Application of biosorption for the removal of organic pollutants: A review. *Process Biochem.* **2005**, *40*, 997–1026. [[CrossRef](#)]
3. Santos, S.C.R.; Boaventura, R.A.R. Adsorption modeling of textile dyes by sepiolite. *Appl. Clay Sci.* **2008**, *42*, 137–145. [[CrossRef](#)]
4. Franca, D.G.R.; Vieira, A.; Mata, A.M.T.A.; Carvalho, S.G.; Pinheiro, H.M.; Lourenço, D.N. Effect of an azo dye on the performance of an aerobic granular sludge sequencing batch reactor treating a simulated textile wastewater. *Water Res.* **2015**, *85*, 327–336. [[CrossRef](#)] [[PubMed](#)]
5. Li, C.S.; Tang, Y.P.; Kang, B.N.; Wang, B.S.; Zhou, F.; Ma, Q.; Xiao, J.; Wang, D.Z.; Liang, J. Photocatalytic degrading methyl orange in water phase by UV-irradiated CdS carried by carbon nanotubes. *Sci. China Ser. E* **2007**, *50*, 279–289. [[CrossRef](#)]
6. Soltani, T.B.; Entezari, M.H. Sono-synthesis of bismuth ferrite nanoparticles with high photocatalytic activity in degradation of Rhodamine B under solar light irradiation. *Chem. Eng. J.* **2013**, *223*, 145–154. [[CrossRef](#)]
7. Gupta, V.K.; Suhas. Application of low-cost adsorbents for dye removal—A review. *J. Environ. Manag.* **2009**, *90*, 2313–2342. [[CrossRef](#)] [[PubMed](#)]
8. Wu, J.; Ma, L.M.; Chen, Y.L.; Cheng, Y.Q.; Liu, Y.; Zha, X.S. Catalytic ozonation of organic pollutants from bio-treated dyeing and finishing wastewater using recycled waste iron shavings as a catalyst: Removal and pathways. *Water Res.* **2016**, *92*, 140–148. [[CrossRef](#)] [[PubMed](#)]
9. Li, Y.H.; Du, Q.J.; Liu, T.H.; Qi, Y.; Zhang, P.; Wang, Z.H.; Xia, Y.Z. Preparation of activated carbon from enteromorphaprolifera and its use on cationic red X-GRL removal. *Appl. Surf. Sci.* **2011**, *257*, 10621–10627. [[CrossRef](#)]
10. Coasne, B.; Alba-Simionesco, C.; Audonnet, F.; Dosseh, G.; Gubbins, K.E. Adsorption, structure and dynamics of benzene in ordered and disordered porous carbons. *Phys. Chem. Chem. Phys.* **2011**, *13*, 3748–3757. [[CrossRef](#)] [[PubMed](#)]
11. Du, Q.J.; Sun, J.K.; Li, Y.H.; Yang, X.X.; Wang, X.H.; Wang, Z.H.; Xia, L.H. Highly enhanced adsorption of congo red onto graphene oxide/chitosan fibers by wet-chemical etching off silica nanoparticles. *Chem. Eng. J.* **2014**, *245*, 99–106. [[CrossRef](#)]
12. Chen, L.; Li, Y.H.; Hu, S.; Sun, J.K.; Du, Q.J.; Yang, X.X.; Ji, Q.; Wang, Z.H.; Wang, D.C.; Xia, Y.Z. Removal of methylene blue from water by cellulose/grapheme oxide fibres. *J. Exp. Nanosci.* **2016**, *11*, 1156–1170. [[CrossRef](#)]
13. Sadrnourmohamadi, M.; Gorczyca, B. Removal of dissolved organic carbon (DOC) from high DOC and hardness water by chemical coagulation: Relative importance of monomeric, polymeric, and colloidal aluminum species. *Sep. Sci. Technol.* **2015**, *50*, 2075–2085. [[CrossRef](#)]
14. Kumar, R.V.; Ghoshal, A.K.; Pugazhenthii, G. Fabrication of zirconia composite membrane by in situ hydrothermal technique and its application in separation of methyl orange. *Ecotoxicol. Environ. Saf.* **2015**, *121*, 73–79. [[CrossRef](#)] [[PubMed](#)]

15. Gopakumar, D.A.; Pasquini, D.; Henrique, M.A.; Morais, L.C.D.; Grohens, Y.; Thomas, S. Meldrum's Acid Modified Cellulose Nanofiber-Based Polyvinylidene Fluoride Microfiltration Membrane for Dye Water Treatment and Nanoparticle Removal. *ACS Sustain. Chem. Eng.* **2017**, *5*, 2026–2033. [[CrossRef](#)]
16. Gulshan, F.; Yanagida, S.; Kameshima, Y.; Isobe, T.; Nakajima, A.; Okada, K. Various factors affecting photodecomposition of methylene blue by iron-oxides in an oxalate solution. *Water Res.* **2010**, *44*, 2876–2884. [[CrossRef](#)] [[PubMed](#)]
17. Dong, Y.M.; Tang, D.Y.; Li, C.S. Photocatalytic oxidation of methyl orange in water phase by Immobilized TiO₂-carbon nanotube nanocomposite photocatalyst. *Appl. Surf. Sci.* **2014**, *296*, 1–7. [[CrossRef](#)]
18. El-Naas, M.H.; Al-Muhtaseb, S.A.; Makhoulf, S. Biodegradation of phenol by pseudomonas putida immobilized in polyvinyl alcohol (PVA) gel. *J. Hazard. Mater.* **2009**, *164*, 720–725. [[CrossRef](#)] [[PubMed](#)]
19. Bagheri, S.; Termeh, Y.A.; Do, T.O. Photocatalytic pathway toward degradation of environmental pharmaceutical pollutants: Structure, kinetics and mechanism approach. *Catal. Sci. Technol.* **2017**, *7*, 4548–4569. [[CrossRef](#)]
20. Singh, K.; Arora, S. Removal of Synthetic Textile Dyes from Wastewaters: A Critical Review on Present Treatment Technologies. *Crit. Rev. Environ. Sci. Technol.* **2011**, *41*, 807–878. [[CrossRef](#)]
21. Yagub, M.T.; Sen, T.K.; Afroze, S.; Ang, H.M. Dye and its removal from aqueous solution by adsorption: A review. *Adv. Colloid Interface Sci.* **2014**, *209*, 172–184. [[CrossRef](#)] [[PubMed](#)]
22. Mezohegyi, G.; Zee, F.P.; Font, J.; Fortuny, A.; Fabregat, A. Towards advanced aqueous dye removal processes: A short review on the versatile role of activated carbon. *J. Environ. Manag.* **2012**, *102*, 148–164. [[CrossRef](#)] [[PubMed](#)]
23. Chuah, T.G.; Jumariah, A.; Azni, I.; Katayon, S.; Thomas, C.S.Y. Rice husk as a potentially low-cost biosorbent for heavy metal and dye removal: An overview. *Desalination* **2005**, *175*, 305–316. [[CrossRef](#)]
24. Nag, A.; Gupta, N.; Biswas, M.N. Removal of chromium(VI) and arsenic(III) by chemically treated saw dust. *Indian J. Environ. Prot.* **1999**, *19*, 25–31.
25. Verma, S.; Nadagouda, M.N.; Varma, R.S. Porous nitrogen-enriched carbonaceous material from marine waste: Chitosan-derived carbon nitride catalyst for aerial oxidation of 5-hydroxymethylfurfural (HMF) to 2,5-furandicarboxylic acid. *Sci. Rep.* **2017**, *7*, 13596. [[CrossRef](#)] [[PubMed](#)]
26. Yang, J.J.; Chen, D.M.; Zhu, Y.; Zhang, Y.M.; Zhu, Y.F. 3D-3D porous Bi₂WO₆/graphene hydrogel composite with excellent synergistic effect of adsorption-enrichment and photocatalytic degradation. *Appl. Catal. B* **2017**, *205*, 228–237. [[CrossRef](#)]
27. Leary, R.; Westwood, A. Carbonaceous nanomaterials for the enhancement of TiO₂ photocatalysis. *Carbon* **2011**, *49*, 741–772. [[CrossRef](#)]
28. Verma, S.; Baig, R.N.; Nadagouda, M.N.; Varma, R.S. Aerobic oxidation of alcohols in visible light on Pd-grafted Ti cluster. *Tetrahedron* **2017**, *73*, 5577–5580. [[CrossRef](#)]
29. Gao, F.; Chen, X.Y.; Yin, K.; Dong, S.; Ren, Z.F.; Yuan, F.; Yu, T.; Zou, Z.G.; Liu, J.M. Visible-Light Photocatalytic Properties of Weak Magnetic BiFeO₃ Nanoparticles. *Adv. Mater.* **2007**, *19*, 2889–2892. [[CrossRef](#)]
30. Bai, X.F.; Wei, J.; Tian, B.; Liu, Y.; Reiss, T.; Guiblin, N.; Gemeiner, P.; Dkhil, B.; Infante, C.I. Size Effect on Optical and Photocatalytic Properties in BiFeO₃ Nanoparticles. *J. Phys. Chem. C* **2016**, *120*, 3595–3601. [[CrossRef](#)]
31. Wang, N.; Zhu, L.H.; Lei, M.; She, Y.B.; Cao, M.J.; Tang, H.Q. Ligand-Induced Drastic Enhancement of Catalytic Activity of Nano-BiFeO₃ for Oxidative Degradation of Bisphenol A. *ACS Catal.* **2011**, *1*, 1193–1202. [[CrossRef](#)]
32. Luo, W.; Zhu, L.H.; Wang, N.; Tang, H.Q.; Cao, M.J.; She, Y.B. Efficient Removal of Organic Pollutants with Magnetic Nanoscaled BiFeO₃ as a Reusable Heterogeneous Fenton-Like Catalyst. *Environ. Sci. Technol.* **2010**, *44*, 1786–1791. [[CrossRef](#)] [[PubMed](#)]
33. Xiang, Q.J.; Yu, J.G.; Jaroniec, M. Graphene-based semiconductor photocatalysts. *Chem. Soc. Rev.* **2012**, *41*, 782–796. [[CrossRef](#)] [[PubMed](#)]
34. Liang, J.; Li, X.M.; Yu, Z.G.; Zeng, G.M.; Luo, Y.; Jiang, L.B.; Yang, Z.X.; Qian, Y.Y.; Wu, H.P. Amorphous MnO₂ Modified Biochar Derived from Aerobically Composted Swine Manure for Adsorption of Pb(II) and Cd(II). *ACS Sustain. Chem. Eng.* **2017**, *5*, 5049–5058. [[CrossRef](#)]
35. Wu, Y.J.; Zhang, L.J.; Gao, C.L.; Ma, J.Y.; Ma, X.H.; Han, R.P. Adsorption of copper ions and methylene blue in a single and binary system on wheat straw. *J. Chem. Eng. Data* **2009**, *54*, 3229–3234. [[CrossRef](#)]

36. Parida, K.M.; Sahu, S.; Reddy, K.H.; Sahoo, P.C. A kinetic, thermodynamic: And mechanistic approach toward adsorption of methyleneblue over water-washed manganese nodule leached residues. *Ind. Eng. Chem. Res.* **2011**, *50*, 843–848. [[CrossRef](#)]
37. Hana, R.P.; Zhang, J.J.; Han, P.; Wang, Y.F.; Zhao, Z.H.; Tang, M.S. Study of equilibrium, kinetic and thermodynamic parameters about methylene blue adsorption onto natural zeolite. *Chem. Eng. J.* **2009**, *145*, 496–504. [[CrossRef](#)]
38. Cazetta, A.L.; Pezoti, O.; Bedin, K.C.; Silva, T.L.; Junior, A.P.; Asefa, T.; Almeida, V.C. Magnetic Activated Carbon Derived from Biomass Waste by Concurrent Synthesis: Efficient Adsorbent for Toxic Dyes. *ACS Sustain. Chem. Eng.* **2016**, *4*, 1058–1068. [[CrossRef](#)]
39. Chen, B.L.; Yang, Z.X.; Ma, G.P.; Kong, D.L.; Xiong, W.; Wang, J.B.; Zhu, Y.Q.; Xia, Y.D. Heteroatom-doped porous carbons with enhanced carbon dioxide uptake and excellent methylene blue adsorption capacities. *Microporous Mesoporous Mater.* **2018**, *257*, 1–8. [[CrossRef](#)]
40. Zhou, Q.Y.; Jiang, X.; Guo, Y.H.; Zhang, G.C.; Jiang, W.J. An ultra-high surface area mesoporous carbon prepared by a novel MnO-templated method for highly effective adsorption of methylene blue. *Chemosphere* **2018**, *201*, 519–529. [[CrossRef](#)] [[PubMed](#)]
41. Nasrullah, A.; Bhat, A.H.; Naeem, A.; Isa, M.H.; Danish, M. High surface area mesoporous activated carbon-alginate beads for efficient removal of methylene blue. *Int. J. Biol. Macromol.* **2018**, *107*, 1792–1799. [[CrossRef](#)] [[PubMed](#)]
42. Li, C.S.; Wang, D.Z.; Liang, T.X.; Wang, X.F.; Wu, J.J.; Hu, X.Q.; Liang, J. Oxidation of multiwalled carbon nanotubes by air: Benefits for electric double layer capacitors. *Powder Technol.* **2004**, *142*, 175–179. [[CrossRef](#)]
43. Li, C.S.; Wang, D.Z.; Liang, T.X.; Wang, X.F.; Liang, J. A study of activated carbon nanotubes as Double-Layer Capacitors electrode materials. *Mater. Lett.* **2004**, *58*, 3774–3777. [[CrossRef](#)]
44. Körbahti, B.K. Response surface optimization of electrochemical treatment of textile dye wastewater. *J. Hazard. Mater.* **2007**, *145*, 277–286. [[CrossRef](#)] [[PubMed](#)]
45. Langmuir, I. The adsorption of gases on plane surfaces of glass, mica and platinum. *J. Am. Chem. Soc.* **1918**, *40*, 1361–1403. [[CrossRef](#)]
46. Freundlich, H.M.F. Over the adsorption in solution. *J. Phys. Chem.* **1906**, *57*, 385–470.
47. Bulut, E.; Ozacar, M.; Sengil, I.A. Equilibrium and kinetic data and process design for adsorption of Congo Red onto bentonite. *J. Hazard. Mater.* **2008**, *154*, 613–622. [[CrossRef](#)] [[PubMed](#)]
48. Chen, M.; Chen, Y.; Diao, G.W. Adsorption kinetics and thermodynamics of methylene blue onto p-tert-butyl-calix[4,6,8] arene-bonded silica gel. *J. Chem. Eng. Data* **2010**, *55*, 5109–5116. [[CrossRef](#)]
49. Dutta, S.; Bhattacharyya, A.; Ganguly, A.; Gupta, S.; Basu, S. Application of Response Surface Methodology for preparation of low-cost adsorbent from citrus fruit peel and for removal of Methylene Blue. *Desalination* **2011**, *275*, 26–36. [[CrossRef](#)]
50. Wu, X.P.; Xu, Y.Q.; Zhang, X.L.; Wu, Y.C.; Gao, P. Adsorption of low-concentration methylene blue onto a palygorskite/carbon composite. *New Carbon Mater.* **2015**, *30*, 71–78. [[CrossRef](#)]
51. Yang, J.M. A facile approach to fabricate an immobilized-phosphate zirconium-based metal-organic framework composite (UiO-66-P) and its activity in the adsorption and separation of organic dyes. *J. Colloid Interface Sci.* **2017**, *505*, 178–185. [[CrossRef](#)] [[PubMed](#)]
52. Yan, L.G.; Yang, K.; Shan, R.R.; Yan, T.; Wei, J.; Yu, S.J.; Yu, H.Q.; Du, B. Kinetic, isotherm and thermodynamic investigations of phosphate adsorption onto core-shell Fe₃O₄@LDHs composites with easy magnetic separation assistance. *J. Colloid Interface Sci.* **2015**, *448*, 508–516. [[CrossRef](#)] [[PubMed](#)]
53. Marrakchi, F.; Auta, M.; Khanday, W.A.; Hameed, B.H. High-surface-area and nitrogen-rich mesoporous carbon material from fishery waste for effective adsorption of methylene blue. *Powder Technol.* **2017**, *321*, 428–434. [[CrossRef](#)]
54. Doğan, M.; Alkan, M.; ÖDemirbaş, Ö.; Özdemir, Y.; Özmetin, C. Adsorption kinetics of maxilon blue GRL onto sepiolite from aqueous solutions. *Chem. Eng. J.* **2006**, *124*, 89–101. [[CrossRef](#)]
55. Ho, Y.S. Second-order kinetic model for the sorption of cadmium onto tree fern: A comparison of linear and non-linear methods. *Water Res.* **2006**, *40*, 119–125. [[CrossRef](#)] [[PubMed](#)]
56. Li, C.S.; Zhang, B.Y.; Chen, X.J.; Hu, X.Q.; Liang, J. Enhancing the crystalline degree of carbon nanotubes by acid treatment, air oxidization and heat treatment. *J. Univ. Sci. Technol. B* **2005**, *12*, 38–42.

57. Shen, Y.; Fang, Q.L.; Chen, B.L. Environmental applications of three-dimensional graphene-based macrostructures: Adsorption, transformation, and detection. *Environ. Sci. Technol.* **2015**, *49*, 67–84. [[CrossRef](#)] [[PubMed](#)]
58. Wu, Z.; Zhong, H.; Yuan, X.Z.; Wang, H.; Wang, L.L.; Chen, X.H.; Zeng, G.M.; Wu, Y. Adsorptive removal of methylene blue by rhamnolipid-functionalized graphene oxide from wastewater. *Water Res.* **2014**, *67*, 330–344. [[CrossRef](#)] [[PubMed](#)]
59. Cheng, M.; Zeng, G.M.; Huang, D.L.; Lai, C.; Liu, Y.; Zhang, C.; Wang, R.Z.; Qin, L.; Xue, W.J.; Song, B.; et al. High adsorption of methylene blue by salicylic acid–methanol modified steel converter slag and evaluation of its mechanism. *J. Colloid Interface Sci.* **2018**, *515*, 232–239. [[CrossRef](#)] [[PubMed](#)]
60. Sun, N.; Qu, Y.; Chen, S.Y.; Yan, R.; Humayun, M.; Liu, Y.D.; Bai, L.L.; Jing, L.Q.; Fu, H.G. Efficient photodecomposition of 2,4-dichlorophenol on recyclable phase-mixed hierarchically structured Bi₂O₃ coupled with phosphate-bridged nano-SnO₂. *Environ. Sci. Nano* **2017**, *4*, 1147–1154. [[CrossRef](#)]
61. Li, C.S.; Wang, D.Z.; Wang, X.F.; Liang, J. Controlled electrochemical oxidation for enhancing the capacitance of carbon nanotube composites. *Carbon* **2005**, *43*, 1557–1560. [[CrossRef](#)]



© 2018 by the authors. Licensee MDPI, Basel, Switzerland. This article is an open access article distributed under the terms and conditions of the Creative Commons Attribution (CC BY) license (<http://creativecommons.org/licenses/by/4.0/>).